How do hydrogen atoms on surfaces affect the trajectories of heavier scattered atoms?

K. M. Lui,[a] I. Bolotin, A. Kutana, V. Bykov, W. M. Lau,[a] and J. W. Rabalais[b]
Department of Chemistry, University of Houston, Houston, Texas 77204-5641

(Received 4 August 1999; accepted 29 September 1999)

The recently developed technique of scattering and recoiling imaging spectrometry (SARIS) is used to probe the effect of hydrogen atoms on the trajectories of 5 keV Ne^+ scattering from a Pt(111) surface. Classical kinematic calculations and ion trajectory simulations, using the scattering and recoiling imaging code (SARIC), are carried out in order to probe the details of the interaction and the nature of the perturbation. It is demonstrated that adsorbed hydrogen atoms are capable of deflecting these low kilo-electron-volt Ne trajectories scattering from a Pt surface. These perturbations result in spatial shifts and broadenings of the anisotropic features of the SARIS images that are readily detectable. The scattered Ne atoms lose 0–18% of their initial kinetic energy as a result of the perturbation by the H atoms. The physics of the perturbation on the trajectories can be understood from straightforward classical kinematic calculations and SARIC ion trajectory simulations. © *1999 American Institute of Physics.* [S0021-9606(99)71148-7]

I. INTRODUCTION

It has recently been shown that ion channeling at low kilo-electron-volt energies is a sensitive probe for determining the adsorption site of hydrogen on surfaces.[1] Using time-of-flight scattering and recoiling spectrometry (TOF-SARS)[2] in a backscattering geometry where the angle between the incident ions and the channel axis is less than the Lindhard critical angle,[3] the Lindhard criteria are satisfied and ion channeling is observed. Under these conditions, the atomic potentials of the individual atoms making up the walls of the channel overlap to form a continuous potential and strongly correlated small angle collisions prevail. When the angle between the incident ions and the channel axis is increased beyond the critical angle, large angle deflections result from the more corrugated potential surfaces. This gives rise to a flux of backscattered particles that have experienced only single or quasisingle collisions with energies predictable by the binary collision approximation.[4] This outgoing flux acts as a probe of foreign atoms adsorbed in an ordered array on the crystal surface. By performing the channeling along different crystallographic directions, the position of adsorbed atoms can be derived unambiguously by a triangulation procedure. Using a 5 keV Ne^+ beam for channeling, quantitative analysis of the Pt(111)-(1×1)-H surface has shown[1] that the hydrogen atoms preferentially populate the fcc site at a height of 0.9 ± 0.1 Å above the first-layer Pt atoms. This result is in excellent agreement with previous experimental measurements[5] and theoretical calculations[6] for this system.

Although the presence of hydrogen atoms on a surface is generally considered to present only a minor perturbation on the scattering trajectories of heavy atoms, the recent channeling measurements show that the hydrogen atoms can perturb the trajectories of heavier projectiles such as Ne to a detectable level. Since low energy ion channeling is capable of probing the positions of light elements on heavy substrates with analysis by simple geometrical constructs, its development as a structural analysis technique that is complementary to Rutherford backscattering (RBS) requires understanding the physics of how hydrogen atoms on surfaces affect the trajectories of heavier scattered atoms.

This paper uses the recently developed technique of scattering and recoiling imaging spectrometry (SARIS)[7] to probe the affect of hydrogen atoms on the trajectories of 5 keV Ne^+ scattering from a Pt(111) surface. The images clearly demonstrate that the Ne trajectories are bent to detectable levels by the presence of hydrogen atoms. Classical kinematic calculations and trajectory simulations, using the scattering and recoiling imaging code (SARIC),[8] are carried out in order to probe the details of the interaction and the nature of the perturbation.

II. EXPERIMENT

A. SARIS measurements

The SARIS experiment is similar to time-of-flight scattering and recoiling spectrometry (TOF-SARS)[2] except that it uses a large area position-sensitive microchannel plate (MCP) detector to capture element-, velocity-, and spatially resolved images of scattered and recoiled atoms simultaneously. An ion beam line that delivers pulsed, mass-selected noble gas ions in the range 1–10 keV with an ion flux of ~1 pA/cm^2 and a pulse rate of ~30 kHz is used. The detector is a 75×95 mm^2 chevron type MCP with resistive anode encoder. The MCP is gated so that the data are collected in time frames of 16.7 ns in order to resolve the quasisingle scattering features. Details have been described elsewhere.[9]

[a]Permanent address: Department of Physics, The Chinese University of Hong Kong, Shatin, N. T., Hong Kong, China.
[b]Author to whom all correspondence should he addressed; electronic mail: rabalais@jetson.uh.edu

In the present study, 5 keV Ne^+ ions were used to scatter from the Pt(111)-(1×1) surface. Measurements were made by fixing the beam incident angle to $\alpha=19°$ relative to the (111) crystal plane, the MCP normal at its center to a scattering angle of $\theta=24°$, and the distance from the sample to the MCP center to 17 cm. This configuration allows the detector to cover 21° of exit angle β space and 24° of azimuthal angle δ space. The individual SARIS images used for construction of the SARIgrams were collected at a TOF of 0.78 μs, corresponding to quasisingle scattering of Ne from Pt. These images were collected for every 5° of azimuthal rotation of the crystal, resulting in a total of 32 chronological sequences, with each sequence being composed of 255 time frames of 16.7 ns duration.

B. Pt(111) sample

The Pt(111) crystal, in the form of a disk (1×6 mm) with the surface polished within 0.5° of the [111] direction, was cleaned by annealing to 900 K in 10^{-6} Torr O_2 followed by annealing for several hours in ultrahigh vacuum. A sharp 1×1 low energy electron diffraction pattern was observed and no impurities were detectable by TOF-SARS after this treatment. Atomic force microscopy (AFM) measurements exhibited an atomically flat surface with terrace widths of ~100 Å and step heights of one lattice spacing, corresponding to a terrace/step atom ratio of $\sim 10^2$. Adsorption of hydrogen on the Pt surface was accomplished at 300 K by exposure to hydrogen ions (both H^+ and H_2^+) from an ion bombardment gun (500 eV, 10^{12} ions/cm^2 s, 3.6×10^{15} ions/cm^2 dose) using a H_2 backfill at 10^{-5} Torr. The upper bound of the hydrogen coverage, as estimated from the isobars of Norton, Davies, and Jackman,[10] was ~0.15 ML (1 ML=1.5×10^{15} atoms/cm^2).

III. COMPUTATIONS

A. Scattering and recoiling image mapping

Individual SARIS images corresponding to quasisingle scattering events of the projectiles acquired for the Pt(111) surface at different azimuthal angles were merged as follows. Consider an imaginary hemispherical detector with the sample surface at the center of the hemisphere. Since the MCP is in the shape of a planar rectangle whose surface is tangent to the hemispherical surface, the coordinates of the experimental images from the MCP must be transformed to the corresponding coordinates on a hemisphere. Experimental scattering and recoiling intensity distributions collected by the MCP are mapped to the imaginary hemisphere and a contour plot is formed by projecting the spatial intensity distribution onto the plane of the hemisphere base using the azimuthal equidistant projection[11] method. The intensity distribution $I(\delta,\beta)$ of a SARIS image transformed in this manner is called a ''SARIgram''. It allows the SARIS data to be presented in the form of a contour plot with angular coordinate equal to the crystal azimuthal angle δ and the radial coordinate equal to the polar exit angle β. SARIgrams are real-space representations of the crystal structure that carry salient symmetry information about the crystal surface. The image areas of low intensity, i.e., blocking cones, appear as nearly circular features or arcs, reflecting the fact that a normal cross section of such a cone is indeed a circle. There is a close resemblance between the pole figures[12] used in x-ray diffraction, which are stereographic projections, and the SARIgram. Stereographic projections from x-ray diffraction are reciprocal-space representations of crystal structure viewed from above the virtual hemispherical detector. SARIgrams are real-space representations of crystal structure viewed from the sample surface toward the hemispherical detector.

B. Trajectory simulations

Ion trajectory simulations for 5 keV Ne^+ scattering from a Pt(111) surface were carried out with the SARIC[8] program. SARIC is based on the binary collision approximation (BCA) and uses screened Coulomb potentials[13] to simulate the three-dimensional motion of atomic particles. The detailed trajectories of the Ne atoms were simulated by using the molecular dynamics (MD) part of the SARIC code. This MD mode is based on two-body interaction potentials and different types of potentials can be assigned to each of the interacting pair of atoms.

IV. SARIS IMAGES OF CLEAN AND HYDROGEN ADSORBED Pt(111)

A. Clean Pt(111)

Examples of SARIgrams for 5 keV Ne^+ scattered from the clean Pt(111)-(1×1) and Pt(111)-(1×1)-H surfaces are shown in Fig. 1. Individual SARIS images were acquired for the clean and hydrogen adsorbed Pt(111) surfaces using 5 keV Ne^+ and then converted into SARIgrams as described in Sec. III A. For the clean Pt surface, sharp intense features with an apparent 60° periodicity that correspond to focusing of the scattered projectiles by atomic lenses of the crystal surface[7] are observed. These intense features are separated from one another by low intensity regions that originate from blocking cones situated along the exit trajectories of the scattered Ne atoms. Specifically, for this angular configuration, the low intensity regions are due to superposition of blocking cones centered at $\beta=0°$ due to scattered trajectories from first-layer atoms that are blocked by neighboring first-layer atoms as well as cones centered at $\beta>0°$ due to scattering from subsurface atoms and blocking by first-layer atoms. Each of the crystallographic directions indicated on the SARIgram in conjunction with the [111] crystal direction defines a plane of symmetry that bisects the corresponding blocking feature, i.e., the feature is symmetrical about these azimuths. It is observed that the recorded resultant blocking is most pronounced at the [011], [110], and [101] azimuths and appears as only small indentations at the [12$\bar{1}$] and [$\bar{2}$11] azimuths. The angular positions of these three dominant blocking features suggest a sixfold symmetry because they result from only first-layer scattering. Scattering with a higher incidence angle allows sampling of subsurface layers and reveals the threefold symmetry of the (111) surface.

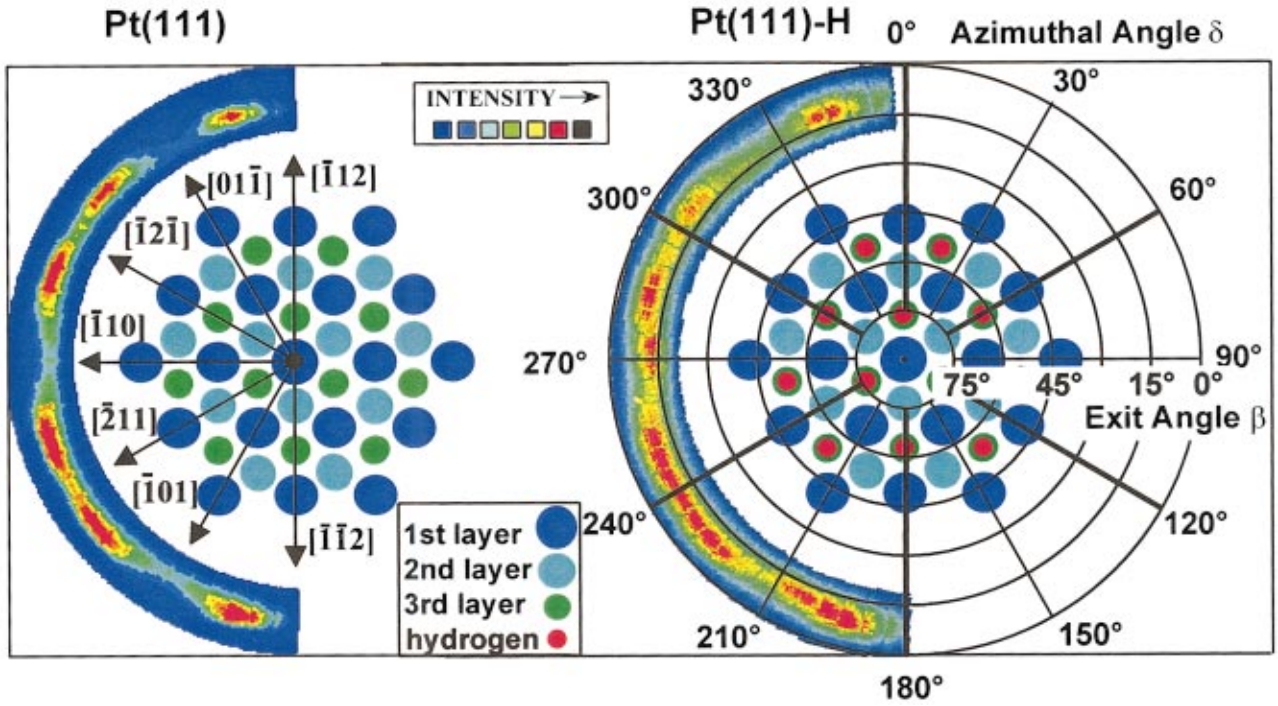

FIG. 1. (Color) SARIgrams for 5 keV Ne^+ scattering from Pt(111) and Pt(111)-(1×1)-H surfaces. The SARIgrams were constructed by using an azimuthal equidistant projection of 32 individual SARIS images. Incident angle $\alpha=19°$, scattering angle to detector normal $\theta=24°$; 17 cm flight path to detector center.

B. Pt(111)-(1×1)-H

The SARIgram of the hydrogen covered Pt(111) surface exhibits similar basic features as those of the clean surface, although severely broadened. It is clear that the aforementioned blocking features are attenuated to different extents. After hydrogen adsorption, the intensity gradients, i.e., $[\partial I(\delta,\beta)/\partial\delta]_{7°<\beta<15°}$, at the azimuthal directions 240° and 300° almost vanish. At the azimuthal directions 210°, 270°, and 330°, these gradients remain large and recongizable, although the features at 270° do not remain as clear as those at 210° and 330°; this is believed to be due to experimental variations during data collection. These observations are in accord with the fact that the H atoms on the surface are capable of deflecting the Ne trajectories by a maximum of ~3°, which amounts to a deflection of ~9 mm on the MCP under the present experimental configuration. Accordingly, the two small indentations at the $[\bar{1}2\bar{1}]$ and $[\bar{2}11]$ azimuths vanish completely.

The importance of the SARIgram of the hydrogen exposed surface is threefold. (1) It demonstrates that H atoms are capable of deflecting Ne atom trajectories and that this deflection can be directly observed. (2) The delocalization of intensities on the SARIgram after hydrogen adsorption infers an increase in the number of scatters per unit cell. (3) The sensitivity to local atomic arrangements provides a direct probe of the adsorption site position of surface hydrogen as will be shown in Sec. V B.

V. DISCUSSION

A. Kinematics of Ne/H scattering

In order to understand the details of the Ne/H scattering system, it is informative to review the kinematics of ion scattering. The basic features[14] of kilo-electron-volt ion–atom collisions can be explained by a classical treatment using the laws of conservation of energy and momentum. An incident ion of mass M_1 and energy E_0 that is scattered from a target atom of mass M_2 into an angle θ has a scattered energy E_s given by

$$E_s/E_0=(1+A)^{-2}[\cos\theta\pm(A^2-\sin^2\theta)^{1/2}]^2, \tag{1}$$

where $A=M_2/M_1$. For $A>1$ only the positive sign applies, while for $1>A>\sin\theta$, both the positive and negative signs are valid. The energy E_r of the recoiled atom is given by

$$E_r/E_0=[4A/(1+A)^2]\cos^2\phi, \tag{2}$$

where ϕ is the recoil angle. For $A<1$ it can be seen from Eq. (1) that the relative energy is a double-valued function of θ and that the maximum or critical scattering angle is given by

$$\theta_c=\sin^{-1}(M_2/M_1). \tag{3}$$

For the case of a Ne atom scattering from a H atom, $\theta_c=2.87°$, as shown in Fig. 2. For $\theta<\theta_c$, the double-valued E_s/E_0 function has one solution for which there is very little energy loss, i.e., $1.0>E_s/E_0>0.91$, and another solution with a larger energy loss, i.e., $0.90>E_s/E_0>0.82$. For ion/atom pairs with a small mass disparity, the low energy branch of Fig. 2 approaches zero. In the Ne/H case, E_s from both branches is high so that they are both detected. The time-of-flight difference for Ne atoms scattered in these two branches, e.g., with $E_s/E_0=1.0$ or 0.82, for $E_0=5$ keV and a flight path of 17 cm is $t\sim80$ ns. Only a single intense Ne scattering peak is observed due to the prevalence of multiple scattering events at the low forward scattering angle used. The differential scattering cross section $\sigma_s(\theta)$ was calculated as a function of θ for both scattering branches using the ZBL

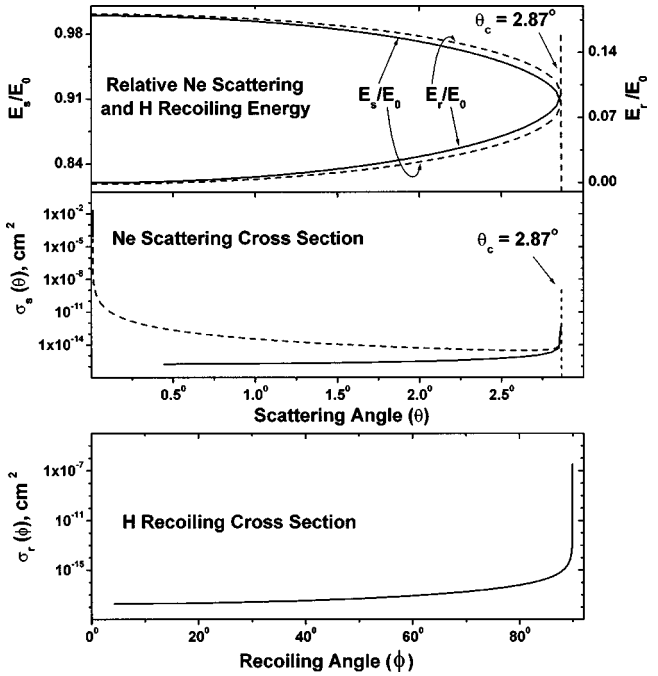

FIG. 2. Plots of the relative Ne scattering E_s/E_0 and H recoiling E_r/E_0 energies and the differential Ne scattering $\sigma(\theta)$ and H recoiling $\sigma(\phi)$ cross sections as a function of the scattering θ and recoiling ϕ angles for 5 keV Ne^+ collisions with a H atom. θ_c is the critical or maximum scattering angle for this projectile—target atom pair. The solid and dashed lines correspond to the positive and negative signs, respectively, of Eq. (1).

potential function. The results, shown in Fig. 2, indicate that the cross section values range from $10^{-16}\,\text{cm}^2 < \sigma_s(\theta) < 10^{-12}\,\text{cm}^2$ for $2.87° > \theta > 0.25°$. These cross sections are sufficiently high that they can cause a noticeable perturbation on the scattered Ne trajectories.

The H atom recoil energy E_r/E_0 and differential recoiling cross section $\sigma_r(\phi)$ were also calculated as a function of ϕ for recoil of the H atoms as shown in Fig. 2. The recoiled H atoms have energies in the range $0 < E_r/E_0 < 0.18\,\text{eV}$. Since the detection efficiency of channel electron multipliers or microchannel plates scales with the particle velocity, the H atoms at the high end of this E_r range are readily detected as recoils as demonstrated elsewhere.[2]

The scattering of Ne atoms by H atoms can be better understood by considering the actual trajectories of the colliding atoms. Figure 3 shows a flux of parallel 5 keV Ne atom trajectories impinging on a H atom. The trajectories of the scattered Ne atoms and the recoiled H atoms are determined by the impact parameter p of the collision. A shadow, or ''shadow cone,'' is formed behind the initial position of the target atom. For $M_2/M_1 > 1$, the shadow cone has a sharp boundary, the scattered atoms are focused at the edges of the cone, and no atoms penetrate into the paraboloidlike volume of the cone. For the H/Ne case where $M_2/M_1 < 1$, some small p collisions result in penetration of the cone by the atom M_1, although a distinct focusing of large p trajectories exists, resulting in a ''semitransparent cone.'' Such semitransparent cones have been observed[15] for hydrogen chemisorbed on a tungsten surface. For $p=0$, the M_1 projectile atoms follow the M_2 target atoms through the center of the cone.

For He and Ar collisions with H atoms, the critical scattering angle θ_c values are 14.48° and 1.43°, respectively. For the H/He combination, θ_c is large and easily detected although $\sigma_s(\theta)$ is relatively small; the opposite situation holds for the H/Ar combination.

B. Interpretation of SARIgrams

The changes in the shapes and intensities of the blocking features in the SARIgrams of Fig. 1 as a result of exposure to hydrogen are a manifestation of (1) the different geometrical interceptions of the respective blocking cones on the detector surface and (2) the proximity of the H atoms to the Ne trajectories. Hydrogen atoms adsorbed at the fcc sites are contained in the planes defined by the [111] and the $[\bar{1}2\bar{1}]$ or $[\bar{2}11]$ crystal directions and situated 0.9 Å above the surface

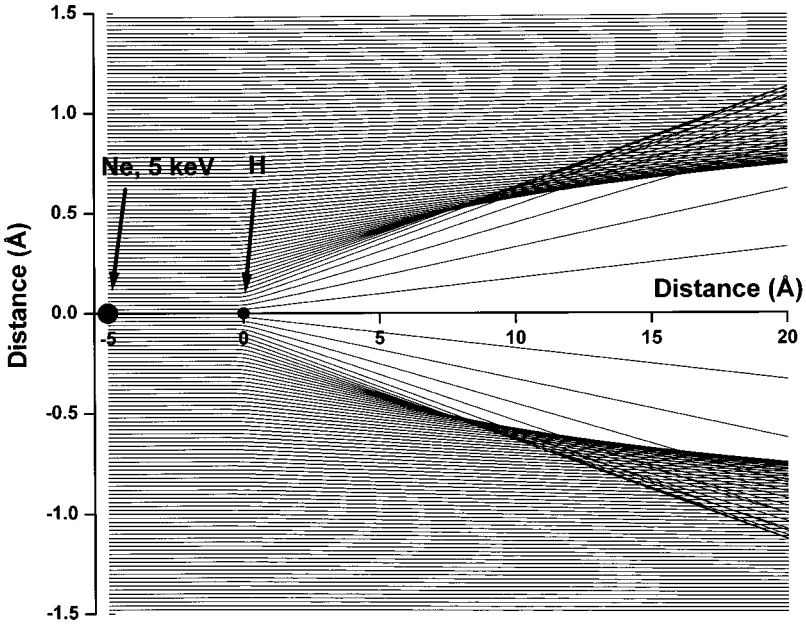

FIG. 3. A flux of parallel 5 keV Ne atom trajectories impinging on a H atom with impact parameters p that are incremented by 0.1 Å.

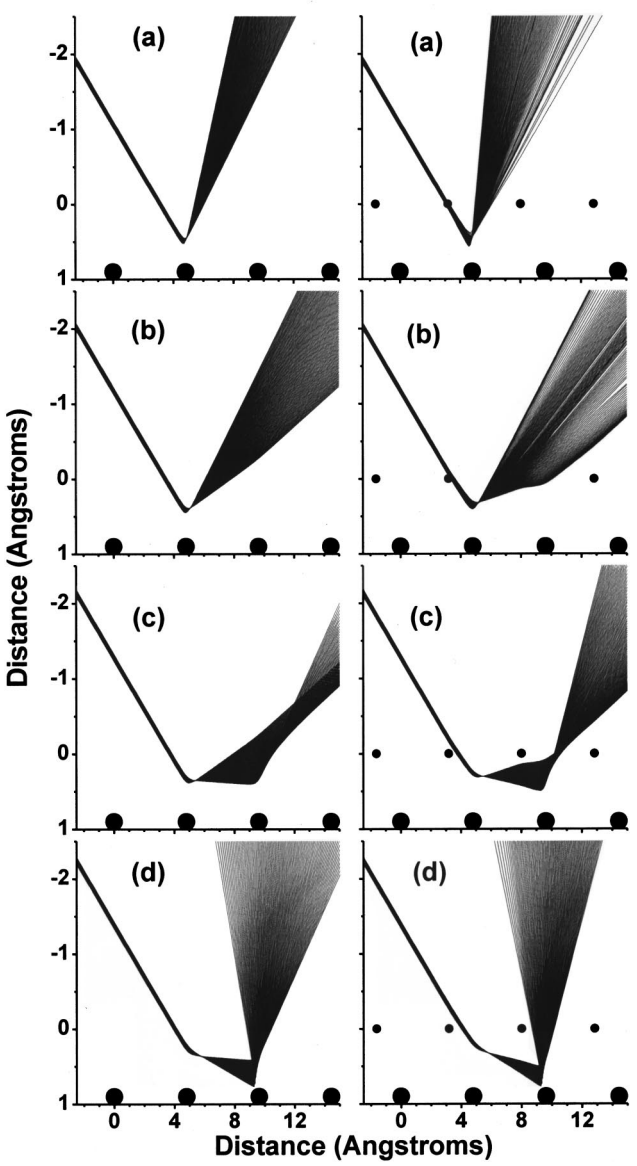

FIG. 4. Molecular dynamics simulation of 5 keV Ne atoms impinging along the [121] azimuth of a clean (left) and hydrogen covered (right) Pt(111) surface. The large and small circles represent Pt and H, respectively. Note that the scales on the ordinate and abscissa are different. The beam incidence angle is $\alpha=19°$ with respect to the surface plane.

plane in the fcc sites as found previously.[1,5,6,10] Therefore, they can directly perturb the incoming and outgoing Ne trajectories along these azimuths. This defocusing by the H atoms results in the large changes observed in Fig. 1 along 240° and 300° in the SARIgram of the hydrogen exposed surface. The features along 210°, 270°, and 330° remain salient after exposure to hydrogen because Ne trajectories scattering along these directions do not make direct collisions with H atoms.

The perturbation of the H atoms on the Ne trajectories can be directly observed by plotting the scattering trajectories along the [121] or [211] crystal directions. Figure 4 illustrates such trajectories for the case of the Ne beam aligned along the [121] azimuth. The Ne atoms impinge from the left with an incidence angle $\alpha=19°$ and the scattered trajectories emerge on the right. The impact parameters of the impinging Ne atoms were incremented by 0.3 Å. When the impact parameter is incremented over a large bombardment segment, the many different scattering trajectories overlap and it is difficult to observe the details of the perturbations caused by the H atoms. As a result, we have separated the impinging Ne atoms into four small bombardment segments in order to more clearly observe these perturbations.

For all of the bombardment segments, it is observed that the presence of H atoms in the fcc position results in deflections of the scattered Ne trajectories. Figure 4(a) represents the case of a bombardment segment that is directly aligned with a H atom. These small impact parameter *p* collisions with H atoms broaden the incoming Ne beam such that the scattered trajectories from the Pt atom are defocused. Figure 4(b) represents the case of a bombardment segment with moderate *p* for the first collision with a H atom and both large and small *p* for the second collision with a H atom. Such double interactions with H atoms result in even larger defocusing effects than the case of Fig. 4(a). Figure 4(c) represents the case of moderate and large *p* for the first and second collisions with H atoms, respectively. Defocusing by the H atoms is clearly observable, even for such large *p* interactions. Perturbations of the trajectories are also observed for the case of two large *p* interactions with H atoms as shown in Fig. 4(d).

The large *p* collisions result in significant deflections of the incoming Ne beam such that the scattered Ne trajectories exhibit large deviations from the focused beams of the clean surface. Since these large *p* collisions occur with the highest probability, these types of trajectories are the dominant contributors to the broadening observed as a result of hydrogen chemisorption. Similar features can be observed along the [211] azimuth. This specific data, however, does not distinguish between chemisorption at the fcc or bcc sites. Low energy ion channeling experiments provide this distinction.[1]

VI. CONCLUSIONS

It is demonstrated that adsorbed hydrogen atoms are capable of deflecting heavy atom (Ne) trajectories scattering from a heavy substrate (Pt) and that this perturbation of the trajectories can be readily detected in SARIS images. The physics of the perturbation on the trajectories can be understood from straightforward classical kinematic calculations and SARIC trajectory simulations. The SARIS and low energy ion channeling techniques[1] are sensitive to low coverages of absorbed hydrogen on surfaces and are capable of quantitatively probing the positions of light elements on heavy substrates with analysis by simple geometrical constructs. The latter capability is a complement to Rutherford backscattering spectrometry.

ACKNOWLEDGMENTS

This material is based on work supported by the National Science Foundation under Grant No. CHE-970665 and the Texas Advanced Research Program under Grant No. 3652-683.

[1] K. M. Lui, Y. Kim, W. M. Lau, and J. W. Rabalais, Appl. Phys. Lett. **75**, 587 (1999).
[2] J. W. Rabalais, Science **250**, 521 (1990); O. Grizzi, M. Shi, H. Bu, and J. W. Rabalais, Rev. Sci. Instrum. **61**, 740 (1990).
[3] J. Lindhard, Mat. Fys. Medd. K. Dan. Vidensk. Selsk. **34**, 14 (1965).
[4] J. W. Rabalais, Crit. Rev. Solid State Mater. Sci. **14**, 319 (1988).
[5] K. Umezawa, T. Ito, M. Asada, S. Nakanishi, P. Ding, W. A. Lanford, and B. Hjorvarsson, Surf. Sci. **387**, 320 (1997); B. J. J. Koeleman, S. T. de Zwart, A. L. Boers, B. Poelsema, and L. K. Verhey, Nucl. Instrum. Methods Phys. Res. **218**, 225 (1983); Phys. Rev. Lett. **56**, 1152 (1986); K. Mortensen, F. Besenbacher, I. Stensgaard, and C. Klink, Surf. Sci. **211/212**, 813 (1989); L. Richter and W. Ho, Phys. Rev. B **36**, 9797 (1987); I. P. Batra, Surf. Sci. **137**, L97 (1984); I. P. Batra, J. A. Barker, and D. J. Auerbach, J. Vac. Sci. Technol. A **2**, 943 (1980); J. Lee, J. P. Cowin, and L. Wharton, Surf. Sci. **130**, 1 (1983); and other references contained in these papers.
[6] P. J. Feibelman and D. R. Hamman, Surf. Sci. **182**, 1987 (411).
[7] C. Kim, C. Höfner, V. Bykov, and J. W. Rabalais, Nucl. Instrum. Methods Phys. Res. B **125**, 315 (1997); C. Höfner, V. Bykov, and J. W.Rabalais;, Surf. Sci. **393**, 184 (1997); C. Kim and J. W. Rabalais, *ibid.* **385**, L938 (1997); C. Kim, J. Ahn, V. Bykov, and J. W. Rabalais, Int. J. Mass Spectrom. Ion Phys **174**, 305 (1998).
[8] V. Bykov, C. Kim, M. M. Sung, K. J. Boyd, S. S. Todorov, and J. W. Rabalais, Nucl. Instrum. Methods Phys. Res. B **114**, 371 (1996); M. M. Sung, V. Bykov, A. Al-Bayati, C. Kim, S. S. Todorov, and J. W. Rabalais, Scanning Microsc. **9**, 321 (1995).
[9] C. Kim, C. Höfner, A. H. Al-Bayati, and J. W. Rabalais, Rev. Sci. Instrum. **69**, 1676 (1998); C. Kim, A. Al-Bayati, and J. W. Rabalais, *ibid.* **69**, 1289 (1998); J. Yao, C. Kim, and J. W. Rabalais, *ibid.* **69**, 306 (1998).
[10] P. R. Norton, J. A. Davies, and T. E. Jackman, Surf. Sci. **121**, 103 (1982).
[11] E. J. Raisz, *Principles of Cartography* (McGraw–Hill, New York, 1962); A. H. Robinson and R. D. Sale, *Elements of Cartography*, 3rd ed. (Wiley, New York, 1969).
[12] B. D. Cullity, *Elements of X-ray Diffraction* (Addison-Wesley, Reading, MA, 1956), p. 275.
[13] J. F. Zeigler, J. P. Biersack, and U. Littmark, in *The Stopping and Range of Ions in Solids*, edited by J. F. Ziegler (Pergamon, New York, 1985).
[14] E. S. Parilis, L. M. Kishnevsky, N. Yu. Turaev, B. E. Baklitzky, F. F. Umarov, M. Kh. Verleger, and I. S. Bitensky, *Atomic Collision on Solids* (North-Holland, Amsterdam, 1993); E. S. Mashkova and V. A. Molchanov, *Medium-Energy Ion Reflection From Solids* (North-Holland, Amsterdam, 1985).
[15] M. Shi, O. Grizzi, H. Bu, J. W. Rabalais, R. R. Rye, and P. Nordlander, Phys. Rev. B **40**, 10163 (1989).